

New determination of the size and bulk density of the binary asteroid 22

Kalliope from observations of mutual eclipses

P. Descamps¹, F. Marchis^{1,2,11}, J. Pollock³, J. Berthier¹, F. Vachier¹, M. Birlan¹, M. Kaasalainen⁴, A.W. Harris⁵, M. Wong², W. Romanishin⁶, E.M. Cooper⁶, K.A. Kettner⁶, P. Wiggins⁷, A. Kryszczyńska⁸, M. Polinska⁸, J.-F. Colliac⁹, A. Devyatkin¹⁰, I. Verestchagina¹⁰, D. Gorshanov¹⁰

¹ Institut de Mécanique Céleste et de Calcul des Éphémérides, Observatoire de Paris, UMR8028 CNRS, 77 av. Denfert-Rochereau 75014 Paris, France

² University of California at Berkeley, Department of Astronomy, 601 Campbell Hall, Berkeley, CA 94720, USA

³ Appalachian State University, Department of Physics and Astronomy, 231 CAP Building, Boone, NC 28608, USA

⁴ Department of Mathematics and Statistics, Gustaf Hallstromin katu 2b, P.O.Box 68, FIN-00014 University of Helsinki, Finland

⁵ DLR Institute of Planetary Research, Rutherfordstrasse 2, 12489 Berlin, Germany

⁶ University of Oklahoma, 440 West Brooks, USA

⁷ Tooele Uuah 84074-9665, USA

⁸ Astronomical Observatory, Adam Mickiewicz University, Sloneczna 36, 60-286 Poznan, Poland

⁹ Observatoire de la Farigourette 13012 Marseille

¹⁰ Central Astronomical Observatory, Pulkovskoe chaussee 65/1, 196140 St.-Petersburg, Russia

¹¹ SETI Institute, 515 N. Whisman Road, Mountain View CA 94043, USA

Pages: 49

Tables: 7

Figures: 14

Corresponding author:

Pascal Descamps

IMCCE, Paris Observatory
77, avenue Denfert-Rochereau
75014 Paris
France

descamps@imcce.fr

Phone: 33 (0)140512268

Fax: 33 (0)146332834

Abstract

In 2007, the M-type asteroid 22 Kalliope reached one of its annual equinoxes. As a consequence, its small satellite Linus orbiting in the equatorial plane underwent a season of mutual eclipses. A dedicated international campaign of observations was organized in order to study several of these scarce events. In this paper we present a summary of the observations and a comprehensive analysis based on a global model of a binary system in mutual eclipse. One of the most significant results is the derivation of a size for Kalliope of 156 ± 4 km, 11% smaller than its IRAS size. As to the diameter of Linus, it is estimated to 28 ± 2 km. This “shortening” of Kalliope is confirmed by the interpretation of earlier observations, such as adaptive optics imaging and those of the stellar occultation of 2006 November, 7. Kalliope appears now as a much more common object with a bulk density of 4.1 ± 0.3 g/cm³ and a macroscopic porosity of ~20-30% typical of that measured for well-known binary main belt systems. Furthermore, we can infer some constraints on the surface composition of W-class asteroids, which are M-class asteroids with the 3 μ m water-of-hydration feature (Rivkin et al., 2000), among which 22 Kalliope is the only member for which we now have a robust derivation of the bulk density.

Keywords

Asteroids, rotation, surfaces – satellites of asteroids - eclipses - photometry

1. Introduction

Ten years ago, Pravec and Hahn (1997) suspected that the near-Earth asteroid 1994 AW1 could be a binary system from the analysis of its complex lightcurve revealed in January 1994. Since that claim, a large number of binary systems have been discovered in all populations of minor bodies in the solar system (Noll, 2006). Extensive and systematic adaptive optics (AO) astrometric follow-up of all known large binary asteroids was performed by our group in order to improve moonlet orbits (Marchis et al., 2003a, 2004). A preliminary solution for the orbit of Linus, satellite of the large ($D_{\text{IRAS}} = 181$ km, Tedesco et al., 2002) main belt asteroid 22 Kalliope, was published (Marchis et al., 2003b). Further AO astrometric observations were carried out up to December 2006 leading to an improvement of the orbit solution (Marchis et al., 2007). Thanks to the precise knowledge of the orbit of Linus, eclipse events were predicted to occur for this binary system from late February through early April 2007 (Descamps et al., 2006). The observation of such events requires a favourable geometry, when the Earth is near the satellite's orbital plane so that eclipses occur at regular intervals. Photometric observation of mutual events is a powerful method to detect and study small asynchronous binaries (Pravec et al. 1998, Mottola and Lahulla, 2000, Ryan et al., 2004, Pravec et al., 2006) as well as doubly synchronous pairs of twin asteroids (Descamps et al., 2007, Marchis et al., 2007a).

Among all asynchronous binary systems with a large primary known so far, the secondary-to-primary size ratio of the 22 Kalliope system is the highest with a value estimated to 0.2 which is considered as the lower photometric detection limit of a binary system in mutual eclipse (Pravec et al., 2006). Since Linus was always beyond the resolving power of the largest Earth-based telescopes (55 mas for the Keck-10m telescope), we know next to nothing of its physical properties. We could roughly estimate at the present time its size indirectly derived by

measuring the secondary to primary flux ratio in AO imaging which bounds it between 20 and 40km (Marchis et al., 2003). With the 2007 favourable circumstances, photometric observations of mutual eclipses enabled us to tightly constrain the physical characteristics of both Linus and Kalliope. This is the result of the first international campaign ever organized to detect predicted mutual eclipses within an asynchronous asteroidal system.

Before tackling in section 3 the issue of detection of mutual eclipses within the photometric observations collected in 2007, we strive to get an improved polyhedral shape model of Kalliope in section 2. This new shape solution along with the refinement of its rotational properties, that is, its spin axis and sidereal period, were input in a comprehensive photometric model (described in section 4) of the eclipses occurring within a tightly bound binary system with a non-spherical primary. This model is applied to the observations in order to carefully interpret them in terms of the physical characteristics of either body. In section 5, we deal with a comparison of the physical properties derived from the present study to those from past observations of different nature. Lastly, we derive in section 6 a new value of the bulk density of Kalliope and discuss its implications as regards to the surface mineralogy and the possible origin of this binary system.

2. Improving the topographic shape model of Kalliope

The shape and pole solution are crucial parameters to predict and account for observed photometric rotational lightcurves. Kaasalainen et al. (2002) derived an initial polyhedral shape solution of 22 Kalliope from their noteworthy lightcurve inversion method (Kaasalainen et al., 2001). This model should be considered as an approximation of the real shape of the primary. The spin axis was derived independently from our updated orbit solution of Linus (Marchis et al., 2007). After collecting observations, spanning nearly 5 years (2001-2006), no change in the

orbit pole has been detected, implying the absence of precession of the orbital plane. Consequently, we can identify both the orbit and spin poles which leads to an adopted spin solution, expressed in J2000 ecliptic coordinates, $\lambda = 197 \pm 2^\circ$ and $\beta = -3 \pm 2^\circ$. This pole solution is mirror from the one adopted in Marchis et al. (2003b) but is similar to one of the two solutions derived by Kaasalainen et al. (2002) who already stated that the more likely solution was the one with $\lambda = 197^\circ$.

From November 2006 to April 2007, a long-term photometric follow-up of Kalliope has been performed with the 0.4m telescope at Appalachian State University's Rankin Science Observatory located in western North Carolina. Images were taken in the R band using an SBIG ST-9e CCD camera and the data were reduced by aperture photometry. The collected lightcurves are displayed on Figure 1. This new set of photometric data was used to get an updated shape, pole and period solution using the aforementioned inversion method. The derived spin vector solution in ecliptic coordinates is $\lambda = 197 \pm 5^\circ$ and $\beta = 3.7^{+4}_{-5}^\circ$, in fairly good agreement with the preceding one, and a sidereal spin period of 4.148199 ± 0.000001 hr. The asteroid model is represented as polyhedrons with triangular surface facets. For the sake of our global photometric model, further described in this paper, the polyhedral shape was converted over a regular grid in latitude-longitude. The resulting model is slightly degraded in this transformation so that our data are matched with an accuracy of about 0.02 magnitudes. Nevertheless the shape model is improved owing to the edge-on aspect of Kalliope, never observed as yet. In this shape fitting process, the photometric contribution of the satellite does not seem to have a significant effect and was consequently neglected. The scattering of solar light from the surface is synthesized considering an empirical Minnaert's law (1941) with a limb darkening parameter k adjusted to 0.62 ± 0.02 , close to that of the icy Galilean satellite Europa, ($k \sim 0.58$, Hestroffer, 2003). The

surface photometric function is an important determinant of the amount of contrast (darkening) for a given topography. The empirical photometric function of Minnaert provides a reasonable working approximation to more complex, physically motivated models such as the Hapke's function (1981) provided the limb-darkening parameter (k) is chosen appropriately as a function of the phase angle. As far as we are concerned, over the involved phase range (2° - 22°), the phase dependence is noticeably low and within the error bars.

The pear-shaped updated result for Kalliope is rendered in Figure 2. Synthetic lightcurves were generated and superimposed on the observations in Figure 1. The agreement with observations is satisfactory and proves the ability of the model to account for the evolving peak-to-peak amplitude together with the overall shapes of lightcurves and the discrepancies between the minima throughout the 6-month photometric follow-up. The new topographic shape model turns out to be slightly more elongated and flattened than previously determined with a theoretical dynamical flattening J_2 of 0.19 instead of 0.15, assuming a uniformly dense body.

3. The mutual events of 2007

3.1 General description

As the orbit of Linus is situated nearly in the equatorial plane of 22 Kalliope, the system undergoes seasons of mutual eclipses and occultations at its equinoxes. This configuration which occurs every 2.5 years happened in the Northern hemisphere spring of 2007. The observation of such events provides opportunities for very precise astrometry of the satellite and studies of its physical characteristics that are not otherwise possible.

Due to the fast-evolving aspect of the system as seen by an Earth observer, the season of mutual

events lasts for only three months. As a result of the distance of 22 Kalliope from the Earth (> 2 AU) and its axial tilt to the ecliptic plane of nearly 90° , mutual eclipses took place in February 2007 and lasted until the beginning of April. The proximity of Kalliope to the Sun in May made observations of the mutual occultations difficult.

The brightness of Kalliope ($m_v = 11$) allowed photometric observations with a small aperture telescope. Anomalous attenuation events were predicted to last about 1 – 3 hrs with detectable amplitude ranging from 0.03 to 0.08 magnitudes (Descamps et al., 2006). The magnitude drop during a total eclipse of Linus, the smaller of the two, mainly depends on the relative sizes. An eclipse of Kalliope by Linus is always partial and the decrease in luminosity will also depend on the shape of Kalliope. We estimated that a photometric accuracy of about 0.01-0.02 was necessary to detect such small photometrical effects

3.2 Observations

The number of observed events depends greatly on the number and geographical distribution of available observers. This is the reason why an international campaign of observation of these events was set up by IMCCE which coordinated the efforts to gather observations of as many of the events as possible¹. The network of observers along with their capabilities are given in the Table 1. Table 2 lists the collected observations during this campaign which started in November 2006 in order to improve beforehand the model of Kalliope alone (cf. section 2). Three events have been detected, of which only one was a total eclipse of Linus on March 8th. For the eclipse of Kalliope on March 17th, the ingress was observed at Haute-Provence observatory, France while the egress was recorded in Oklahoma, USA, so that only two complete events are available altogether.

¹ http://www.imcce.fr/page.php?nav=en/observateur/campagnes_obs/kalliope/index.php

In principle, an eclipse may be identified unambiguously, but in the case of a small satellite the effect is so subtle that it may be confused with the primary's lightcurve. The best way to overcome this difficulty is to bring out a presumed event by subtracting from each other two observations taken a few nights apart so that the residual curve, called the magnitude drop curve, may exhibit a detectable subtle attenuation beyond the observational noise. This process is performed after representing each observation by an expansion in Fourier series, making it possible to carry out a point-to-point subtraction. Data of the night of reference (the night which is supposed not to have an event) are displaced in time according to the period, refined in section 2, and the elapsed time between both observations. The mean residual serves to accurately align in magnitude the data of the second night so that the maxima and minima correspond to those of the first. Figures 3-7 show the resulting negative (3,4) and positive (5-7) detections after applying the described method. On the left side of each figure are two overlapped lightcurves, recorded during two closely spaced sessions, the difference of which is plotted on the right side. Despite the noisy data, prominent light variations are undoubtedly detected on Figures 5, 6, and 7 and reveal ongoing events within the system of Kalliope. The corresponding durations are highlighted on the very lightcurves.

3.3 Approached derivation of the size ratio from the total eclipse of Linus

We can take advantage of the full observation of the total eclipse of Linus by Kalliope. The depth, expressed in magnitudes, of the attenuation is related to the ratio of the components crossed-diameters by the simple formula:

$$\frac{F_s}{F_t} = 2.5 \log(1 + q^2) \quad (1)$$

where q is the secondary-to-primary size ratio, F_s the flux of the secondary, and F_t the total flux. If we apply this formula for an observed attenuation of 0.05mag at the time of disappearance of Linus (Fig.4A), assuming the IRAS diameter of Kalliope of 180 ± 4.5 km (Tedesco et al., 2002), we get a size ratio of 0.21 corresponding to a size of Linus of 38km. This is in pretty good agreement with what it is expected from the flux ratio measured in the adaptive optics observations (Marchis et al., 2003b).

Nevertheless, how reliable such an absolute determination is depends to a great extent on the adopted size of Kalliope. The size of Kalliope is critical to completely assess the physical properties of the system. Besides, we must pay attention to the fact that the curves of magnitude drop do present neither the same pattern nor similar amplitudes. They are not at all reminiscent of the reversed bell curves observed in the case of the mutual events of planetary satellite systems. We may thus wonder whether these features are spurious or not. This is why we should primarily address the matter of modelling the eclipse phenomenon for a trustworthy interpretation of photometric data.

4. Modelling the mutual eclipses

4.1 Description of the synthetic model

From the preliminary work carried out in section 2, we now have a precise knowledge of the

rotation and the shape of the primary. The shape of the secondary cannot be constrained by mutual eclipse observations owing to its smallness relatively to the primary and will be consequently taken as purely spherical. Another point of importance lies on the precise localization of the dark umbral shadow region on the surface of Kalliope whenever it is eclipsed by Linus. This is achieved if we consider that an eclipse is an occultation of one component by another one from the standpoint of a Sun observer. After rotating the whole of the system toward the Sun, the cross sections of the “occluding” and “occulted” bodies, as seen from the Sun, draw outlines which are retrieved and projected onto a same plane of work. Facets of the “occulted” body (the eclipsed body for an Earth observer) which are situated inside or on the border of the “occluding body outline do not receive any illumination. It then remains to return to the initial frame facing the observer – which is that of the tangent plane of the observation - in order to compile the eclipsed facets and to carry out a summation of the intensity over all visible facets. In our model the penumbral annulus is not taken into account because each body is located very close to the other so that the penumbral width is negligible. Light travel time between each body is likewise neglected. The model provides the values of the quantities F_1^e , F_2^e , F_1 and F_2 which stand for the fluxes of Kalliope (subscript 1) and Linus (subscript 2) in and out eclipse. The magnitude drop of an eclipse of Kalliope by Linus (2E1) or an eclipse of Linus by Kalliope (1E2) is straightforwardly provided by the following formula:

$$\Delta F_{1E2} = \frac{F_1 + F_2^e}{F_1 + F_2} \quad (2)$$

$$\Delta F_{2E1} = \frac{F_1^e + F_2}{F_1 + F_2} \quad (3)$$

The eclipse of Linus is said *total* if $F_2^e=0$. Figure 8 shows the apparent configuration of the system generated at the midevent of the eclipse of Kalliope by Linus on March 17th. The dark area on Kalliope, located inside the shadow of Linus, covers an irregular region which is slightly tilted over the path of the shadow. Thus the umbra obliquely falls upon the surface causing for an Earth observer a distortion of the shadow which tends to lengthen and to be curved. Accordingly, the part of flux which is removed from the total collected light is enhanced with respect to that we would have considering a purely spherical primary. This may explain why we observe magnitude drops as large as 0.08mag in the case of eclipses of Kalliope by Linus.

4.2 The effects of the free parameters to be solved

This part is aimed at showing what happens to the theoretical curve of magnitude drop when one parameter is changed while the others are held constant. Thanks to our global model we are now able to scrutinize the effect of the free parameters to be determined in the formation of conspicuous features on the curve of magnitude drop. The only free parameters which are taken into consideration are the sizes of both body and the Linus orbit pole. They are the only determinants of the amplitude and form of the light attenuation during an eclipse event.

4.2.1 The effects of the sizes

As expected, from the Figure 9A-9B, increasing the size of the secondary or decreasing that of the primary make the curves of magnitude drop deeper. We could therefore think that the effects caused by changing one size could be offset by changing the value of other size. However the size of the primary has opportunely a one-to-one effect on the duration of the event and the shape of the curve. As a matter of fact, the profile of the magnitude drop varies according to the

primary's rotational phase. Though, indeed, the events repeat periodically, they do not occur at the same rotational phase of the primary. Therefore the size parameters may be unambiguously constrained so that the synthetic lightcurves can be adequately tailored to the observations.

4.2.2 The effect of the Linus orbit pole

On Figure 9C we have plotted the magnitude drop curves obtained for small departures of the orbital pole with respect to the nominal position derived in the present work. Prominent variations arise for smaller shifts of the orbital pole to such an extent that no event can even occur for a deviation as small as 2 degrees, in the longitude coordinate (λ), with respect to our adopted solution (see section 2). The changes in the duration of the event and the form of the curves are so tremendous that the observation of an event will severely constrain the orbit pole solution. We can estimate that the required accuracy on the ecliptic λ coordinate is better than 0.2° whereas the magnitude drop is much less sensitive to the β coordinate which remains determined with an accuracy of 2° (not presented on the Figures owing to its weak effect).

4.3 Determination of the sizes of Linus and Kalliope

Figure 10 displays some of the characteristics which may be identified in the observed lightcurves plotted in Figure 9. A unique and best-fit solution was found for each size. The equivalent radius of Kalliope was derived to $78 \pm 2 \text{ km}$ and that of Linus to $14 \pm 1 \text{ km}$. These results are discussed below in section 5 and their physical implications in section 6.

4.4 Astrometric reduction of the eclipses

Table 3 summarizes the characteristics of the observed eclipse events as well as the geometric circumstances. For each event, magnitude drops and times of eclipse ingress and egress are

given.

It is straightforward from our photometric model to infer ancillary astrometric relative positions of Linus in the tangent plane of the observation at the times of eclipse ingress and egress (Table 3). The main errors which affect these positions arise from the accuracy in the determined times of eclipse ingress and egress. At worst, it may be estimated to ± 5 minutes or 4 milliarcseconds (7km) in position. Notwithstanding this fairly good level of accuracy, we failed to significantly improve our orbit solution. (The refined orbital parameters can be found in Table 4). The global RMS error remains on the order of 40mas (70km). In the worst case, we even reach an astrometric error of 100mas (175km). Such a solution may be thought to be quite inaccurate in regard to the requirements to forecast mutual events. Indeed the actual shift between observed and calculated times of an event may amount to 2h. The reason lies in the basic keplerian model used to account for the orbit of Linus which is roughly circular with a semi-major axis of 1099 ± 12 km and an orbital period of 3.5954 ± 0.001 days. A much more advanced dynamical model, taking into account the non-spherical gravitational field of the primary, appears to be necessary to take into account small variations in the orbital motion of Linus. The new higher degree of knowledge of Kalliope shape should set up the departure point for gaining insight into the dynamics of Linus. By leaning on the utmost accuracy of mutual eclipses observations, the structure of the gravitational field of Kalliope can be investigated in turn.

Another point of importance is the detection of a low precessing motion of the orbit plane about the spin axis of Kalliope. If we refer indeed to the Figure 9C, it is clear that an eclipse could happen on March 7th and March 17th provided that the ecliptic λ coordinate be of 197° and 195° respectively to adequately match the observations (see Fig. 10). This slight shift of the orbit pole

over ten days is not really surprising and arises from the secular nodal precession n_Ω which is given by (Brouwer and Clemence, 1961):

$$n_\Omega = -\frac{3}{2} n_0 J_2 \frac{R_p^2 \cos i_0}{a_0^2 (1-e_0^2)} \quad (4)$$

Knowing the second degree coefficient in the spherical harmonic expansion of the gravitational potential, $J_2=0.19$, we may extract the nodal and apsidal rates and the resulting Keplerian mean motion, which slightly differs from the observed mean motion, $n_0=100.287^\circ/\text{day}$ (or a Keplerian period of 3.5897 ± 0.001 days). Considering a circular orbit ($e_0\sim 0$), a small inclination over the equatorial plane of Kalliope, $i_0\sim 2^\circ$, the set of physical parameters (J_2 , R_p) previously obtained as well as the Keplerian orbital parameters a_0 , e_0 and n_0 given in Table 4, we derive a nodal rate $n_\Omega=0.15^\circ/\text{day}$ or about 1.5° in ten days which well squares with the observation. In spite of the expected high accuracy on pole position from the observation of mutual eclipses, we report and confirm a final ecliptic J2000 orbital pole solution $\lambda=197\pm 2^\circ$ and $\beta=-3\pm 2^\circ$ in the table 4 regardless the slight detected precession. Further observing campaigns of mutual events could help to finely study and determine this small precession.

5. Comparison with past observations

To check the validity of the shape and pole solution, we examine in this section observations from various sources with predictions based on the overall physical solution derived in section 4.

5.1 Direct imaging by adaptive optics

The computed Kalliope aspect shown in Figure 11 compares very well with a high resolution adaptive optics image of Kalliope taken on 2004 June 28 with the 8-m VLT-UT4 (Very Large Telescope) and its NACO Adaptive Optics system. The best-fit ellipse of the observation gives an extended object of 116x92 mas while our 78km shape model occupies in the tangent plane a fitted ellipse of 115x82 mas. Thus, it is needless to say that our sized shape model is in good agreement with direct imaging of Kalliope.

5.2 First detection of a stellar occultation by an asteroid satellite

On Nov. 7, 2006, the first stellar occultation by the satellite of an asteroid (Linus) was successfully observed by Japanese observers (Soma et al., 2006) according to a prediction we made just one day before (Berthier et al., 2004). This observation not only confirmed the reliability of our orbit solution but also provided a direct measurement of the size of Linus and a partial outline of the cross-section of Kalliope which gives us the opportunity to compare it with the present shape and size solution.

The analysis of the observation of a stellar occultation consists of converting the timings of the disappearance and reappearance of the occulted star as measured by the observers in segments (called chords) in the occultation plane. The length of each segment is directly proportional to the size of the cross-section of the celestial body seen by the observer and to the relative velocity of the body with respect to the observer. Usually, the size of the cross-section of the body is unknown. The relative velocity is computed from the ephemeris of Kalliope, based on INPOP06 planetary theory (Fienga et al., 2006), which provides a geocentric apparent velocity of $17.466 \pm$

0.001km/s at the epoch of the observation. On the basis of this value and from the timings sent by the observers (Table 5) and listed in Table 6, the inferred chords are plotted in Figure 12. The plain segments show the occultation by Kalliope and Linus, respectively, the dashed lines show the negative observations (i.e. no disappearance of the star).

At the epoch of the occultation (2006-11-6T19:49:26 UTC), the current ephemeris uncertainty (CEU, 1σ RMS) of Kalliope provided by ASTORB (Bowell, 2007) was 30 mas or 40 km. The TYCHO-2 catalogue gives an error on the position of the occulted star of about 17 mas. The shift between the hypothetical centre of the cross-section of Kalliope provided by the chords and the centre of the frame allow us to estimate the global error (contribution of the positional errors of the asteroid and the star) on the prediction of the event. We estimate this error to about 65 km or 48 mas, which is comparable with the positional errors of the star and Kalliope. We had predicted the relative position of Linus with respect to Kalliope to be $x=-0''.17$, $y=0''.21$ in the sky plane. It differs from the observed position by about 3 km along the x axis and 51 km along the y axis. That represents a global error on the position of Linus with respect to. our orbital model of about 51 km or 38 mas.

The observed chords of Linus give us a unique opportunity to estimate the size of the moonlet. The distribution of the chords did not allow us to estimate correctly both axis of the profile of Linus: only the size in the direction of the motion is reliable, while the other can only be bordered. The fit of an elliptical profile on the extremity of the chords (the 5 parameters of the conic being fitted on the weighted extremity) gives a solution having a major axis of about 20 km and a minor axis greater than 14 km and less than 38 km (Fig. 12). These measurements are consistent with the derived equivalent size of 28km from mutual events analysis. The few observed chords of Kalliope do not allow us to estimate the size of its cross-section.

Nevertheless it is sufficient to compare the topographic shape models of Kalliope. Figure 13 shows us that the IRAS-based outline does not satisfactorily fit the chords, whereas the 78km-based outline adequately does.

5.3 Thermal observation

Tedesco et al. (2002) reported an estimated diameter for 22 Kalliope of 181 ± 5 km, based on radiometric measurements made during four observations by the IRAS telescope; this value is surprisingly $\sim 11\%$ larger than our calculated diameter. On the basis of this larger average diameter result, Marchis et al. (2003b) reported a very high porosity ($\sim 60\%$) for the primary, which is difficult to explain with any realistic model of the asteroid interior.

We retrieved and reanalyzed individually all the relevant IRAS data using the NEATM algorithm described by Harris (1998). We estimated the size, albedo and η for each observation separately (see Table 7). In the NEATM, the parameter η is a modeling parameter, often referred to as the beaming parameter, which is adjusted together with the diameter to obtain the best fit to the observed thermal continuum. By incorporating a variable η value, the NEATM takes into account the effects of thermal inertia and surface roughness (unlike the standard thermal model on which the original IRAS analysis was based). We discarded IRAS observation #2 because it gives an abnormal η value, possibly due to a background star contamination in the $12\ \mu\text{m}$ measured flux. The average NEATM diameter (177 ± 4 km with $p_v=0.15$ and $\eta=0.753\pm 0.042$) is, however, still significantly larger than the one we report in this paper.

Figure 13 shows the geometry of Kalliope's primary at the times of the IRAS data (June 15 and

19, 1983), calculated using the pole solution and 3D-shape described in this work. The asteroid is seen very close to pole-on, meaning that it was observed while showing its largest apparent surface. Using our model mean diameter of 156 km, the calculated effective diameter at the time of the IRAS sightings (~178 km) is very close to the average diameter derived from the IRAS data using NEATM (the effective diameter is the diameter of a sphere with equivalent projected area to that of the asteroid). If we also include a possible thermal contribution of Linus (R=14 km), the calculated effective diameter of the primary is reduced to ~173 km, still close to the NEATM diameter.

In conclusion, it is evident that the diameter of Kalliope was overestimated based on the IRAS observations because the few IRAS radiometric measurements were made while Kalliope was viewed pole on. Our measured diameter of 156 km is in agreement with the NEATM diameter, taking into account the pole solution and 3D-shape reported in this paper.

6. Revised physical characteristics of Kalliope

From the refined orbit solution of Linus in its motion around Kalliope, the bulk density of Kalliope can be inferred. From the Keplerian mean motion n_0 given in Table 4 we can derive the total mass M_T of the system according to the Kepler's third law:

$$n_0^2 a_0^3 = GM_T = GM_K(1+q) \quad (5)$$

where G is the gravitational constant, M_K the mass of Kalliope, $a_0=1099\pm 10$ km the semi-major axis and $q=0.0058$ the mass ratio between Linus and Kalliope assuming a same bulk density for each of them. We get a mass of Kalliope of $8.18\pm 0.26 \times 10^{18}$ Kg. Given our diameter of Kalliope

of 156 ± 4 km we obtain a bulk density $\rho = 4.09 \pm 0.31 \text{ g/cm}^3$ which is about twice the density from the previous determination (Marchis et al., 2003).

Assignment to the “M” taxonomic class is based on moderate albedo ($\sim 0.1-0.3$), the lack of identified spectral features and a flat or slightly red spectral curve across $0.3-2.5 \mu\text{m}$ wavelength range. A sustained effort has been undertaken for many years to understand the compositional nature of M-type asteroids. As a result, iron meteorites with silicate inclusions are likely meteoritic analogues (Prinz et al., 1982, Rivkin et al., 1995, 1997, Magri et al., 2001, Hardersen et al., 2005, Birlan et al., 2007). The degree of silicate inclusions varies significantly but can compose up to $\sim 50\%$ by volume (Prinz et al., 1984). Recently, Rivkin et al. (1995, 2000) suggested a subgroup of M-class asteroids (called the W class) containing those with an absorption feature at $3 \mu\text{m}$ diagnostic of water of hydration. In other terms, members of this new class are hydrated asteroids with surface composition inconsistent with pure metallic iron. 10 from 27 M-type asteroids have been identified as W-class asteroids among which 22 Kalliope is the only one the bulk density of which is known. These authors concluded that the W class asteroids likely have a mineralogy akin to enstatite chondrites (3.36 g/cm^3) or carbonaceous chondrite-like ($3.05-3.75 \text{ g/cm}^3$) with a relatively large fraction of high-albedo hydrated salts at the surface. Given our revised bulk density of Kalliope, the candidate meteoritic analogs should have a grain density no less than $\sim 4 \text{ g/cm}^3$. The only relevant analogs may therefore be more likely either iron meteorites with almost zero microporosity (grain density of $6.99-7.59 \text{ g/cm}^3$) or stony-iron meteorites with silicate-bearing iron (5.0 g/cm^3). If we agree with the meaning of the $3 \mu\text{m}$ water-of-hydration feature, although its reliability is questioned (Gaffey et al., 2002), its detection for Kalliope is further consistent with the idea that it is rocky with a surface composed of stony-irons such as mesosiderites ($4.16-4.22 \text{ g/cm}^3$) or pallasites ($4.82-4.97 \text{ g/cm}^3$) with

significant amounts of metallic iron. Thus the inferred macroscopic porosity would likely be on the order of ~20-30%, typical of extensively fractured or loosely consolidated asteroids (Britt et al., 2002).

In a recent work, Descamps and Marchis (2007) set forth the idea that most of the main belt binary systems with a large primary, which may be considered as rubble-piles, might originate in a rotational fission process chiefly governed by the level of the internal friction. Adopting their notations, we may update the normalized spin rate of Kalliope to $\Omega=0.408\pm 0.004$ and the non-sphericity parameter $\lambda=1.494$, which is the ratio between the moment of inertia of the body with respect to its spin axis and the moment of inertia of the equivalent sphere. The specific angular momentum of the system may then be computed from a handy formula given in the appendix A of their paper, $H=0.261\pm 0.008$ akin to the average value of the observed main belt binary systems. In other words, despite the new physical sketch of Kalliope derived in the present work, the main conclusions as regards to the total angular momentum hold true, that is, the binary system of Kalliope could likely be the outcome of rotational fission provided that it may be classed as a rubble pile asteroid. This means that the macroscopic porosity should be at least of ~30%, corresponding to the adopted lower porosity for loose rubble or soils (Britt et al. 2002), roughly consistent with the above determination based on mineralogy considerations.

Lastly, if we plot in Figure 14, according to Weidenschilling et al. (1989), tidal evolution time scales as a function of the relative separation, and mass ratio, we may put corresponding values derived for Kalliope, $a/R_p = 14.038$ and $q=0.0058$. We have adopted $\mu Q \approx 3 \times 10^{13}$ dynes/cm². The specific energy dissipation function Q is generally ~100. As to the coefficient of rigidity μ , it ranges from 3×10^{10} dynes/cm² (ice) to 5×10^{11} dynes/cm² for uncompressed but well-consolidated

rocky materials (For instance granite has $\mu \sim 3 \times 10^{11} \text{ dynes/cm}^2$). Moderately fractured carbonaceous asteroids (such as Phobos) have $\mu \sim 10^{10} \text{ dynes/cm}^2$. If we adopt μ to be at least $10^{11} \text{ dynes/cm}^2$ for a stony-iron Kalliope, we may bind the evolution time, assuming initial $a/R_p=1$, between ~ 1.0 and ~ 3.0 billion years, making Kalliope as likely one of the most primitive main belt binary systems. This rough estimation can be connected with the supposed, although controversial, cataclysmic bombardment which occurred at around 3.9Gyr in the inner solar system. A recent model tentatively explains the cataclysm as the result of the readjustment of the orbits of giant planets in the outer solar system (Tsiganis et al., 2005, Gomes et al., 2005). The process would have led to a massive delivery of planetesimals to the inner Solar system, and to the disruption of the asteroid belt. After the disruption of its parent body, it could have been imparted enough angular momentum to a proto-Kalliope during or after its accretional phase to ultimately exceed the threshold for rotational fission which is given by the stability limit for a given friction angle (Holsapple, 2004). This threshold would be reached at an observed specific angular momentum of ~ 0.27 corresponding to a friction angle $\phi \sim 11-14^\circ$ (Descamps and Marchis, 2007). Weidenschilling et al. (1989) already invoked such a mechanism to account for the formation of binary asteroids by rotational fission but with the assumption that the threshold is ~ 0.4 . Such a higher threshold requires an impact involving an energy a few tens of times the binding energy of an asteroid so that the probability an asteroid would survive is near zero. With a less restricting requirement as to the threshold, such impacts may have occurred among large asteroids without disrupting the target, resulting in binaries which can only be a small fraction of the main belt total population.

7 Conclusion

In this work new insights into the physical characteristics of Kalliope have been achieved, which do not support its status as the one of the most porous object observed so far. These new conclusions about Kalliope have been achieved after combining the results of various observational techniques. Firstly, adaptive optics observations (Marchis et al., 2003b, Marchis et al., 2007), are the cornerstone of predictions of mutual events and stellar occultations (accessible to amateur astronomers), as they provide precise knowledge of the orbit of the secondary. Secondly, continuous lightcurve observations, combined with a robust and powerful inversion method (Kaasalainen et al., 2001), enable the construction of a robust 3-dimensional shape of the primary. These different sets of observational data have allowed an accurate and self-consistent model of the Kalliope system to be developed, with important implications for its physical characteristics.

We can thus provide a global and accurate solution for Kalliope in terms of size, shape, spin axis, and scattering properties. The main outcome is a revised diameter for Kalliope of 156 ± 4 km, which is substantiated by other observations and a new analysis of existing radiometric data. As a consequence, we derive a bulk density of 4.1 ± 0.3 g/cm³, twice that derived previously, and a much more realistic macroscopic porosity of 20-30% which is far more typical of fractured or even loosely consolidated asteroids. This is the first density derivation of a W-type asteroid (Rivkin et al., 2000) which puts some tight constraints on the surface composition of this subgroup of M-class asteroids.

References

- Berthier, J., Marchis, F., Descamps, P., Hestroffer, D., 2004. Prediction of stellar occultations by satellite of asteroids. *BAAS*, 36, 1142.
- Birlan, M., Vernazza, P., Nedelcu, D.A., 2007. Spectral properties of nine M-type asteroids. *Astron.Astrophys.*, In press.
- Bowell, E., 2007. The asteroid orbital elements database. <ftp://ftp.lowell.edu/pub/elg/astorb.html>
- Britt, D.T., Yeomans, D., Housen, K., Consolmagno, G.J., 2002. Asteroid density, porosity and structure. In *Asteroids III*, W.F. Bottke, A. Cellino, P. Paolicchi, R. Binzel Eds (University of Arizona Press, Tucson), 103-112.
- Brouwer, D., and G.M. Clemence, 1961. *Methods of celestial mechanics*.
- Descamps, P., Marchis, F., Pollock, J., Birlan, M., Vachier, F., and F. Colas, 2006. 2007 mutual events within the binary system of 22 Kalliope. MEOTUS workshop, Paris.
- Descamps, P., Marchis, F., Michalowski, T., Vachier, F., Colas, F., Berthier, J., Assafin, M., Dunckel, P.B., Polinska, M., Pych, W., Hestroffer, D., Miller, K., Vieira-Martins, R., Birlan, M., Teng-Chuen-Yu, J.-P., Peyrot, A., Payet, B., Dorseuil, J., Léonie, Y., and T. Dijoux, 2007. Figure of the double asteroid 90 Antiope from AO and lightcurves observations *Icarus*, 187, 482-499.
- Descamps, P., and F. Marchis., 2007. Angular momentum of binary asteroids: Implications for their possible origin. *Icarus*, in press.
- Ďurech, J., and M. Kaasalainen, 2003. Photometric signatures of highly nonconvex and binary asteroids. *Astron. And Astrophys.* 404, 709-714.
- Fienga, A., Manche, H., Laskar, J., and M. Gastineau, 2006. INPOP06: a new planetary ephemeris. Nomenclature, Precession and New Models in Fundamental Astronomy, 26th meeting of the IAU, Joint Discussion 16, 22-23 August 2006, Prague.
- Gaffey, M.J., Cloutis, E.A., Kelley, M.S., Reed, K.L., 2002. Mineralogy of asteroids. In *Asteroids III*, W. F. Bottke Jr., A. Cellino, P. Paolicchi, and R. P. Binzel (eds), University of Arizona Press, Tucson, 183-204.
- Gomes, R., Levison, H.F., Tsiganis, K., and A. Morbidelli, 2005. Origin of the catastrophic late heavy bombardment period of the terrestrial planets. *Nature*, 435, 466-469.
- Hapke, B.W., 1981. Bidirectional reflectance spectroscopy. 1: Theory. *J. Geophys. Res.*, 86, 3039-3054.

Hardersen, P.S., Gaffey, M.J., and P.A. Abell, 2005. Near-IR spectral evidence for the presence of iron-poor orthopyroxenes on the surfaces of six M-type asteroids. *Icarus*, 175, 141-158.

Harris, A. W., 1998. A Thermal Model for Near-Earth Asteroids. *Icarus*, 131, 291-301.

Hestroffer, D., 2003. Photometry with a periodic grid. II. Results for J2 Europa and S6 Titan. *Astronomy and Astrophysics*, 403, 749-756.

Holsapple, K.A, 2004. Equilibrium figures of spinning bodies with self-gravity. *Icarus* 172, 272-303.

Kaasalainen, M., Torppa, J., and K. Muinonen, 2001. Optimization methods for asteroid lightcurve inversion. II. The complete inverse problem. *Icarus*, 153, 37-51.

Kaasalainen, M., Torppa, J. and J. Piironen, 2002. Models of twenty asteroids from photometric data. *Icarus*, 159, 369-395.

Magri, C., Consolmagno, G.J., Ostro, S.J., Benner, L.A.M., and B.R. Beeny, 2001. Radar constraints on asteroid regolith properties using 433 Eros as ground truth. *Meteorit. Planet. Sci* 36, 1697-1709.

Marchis, F., Descamps, P., Berthier, J., Hestroffer, D., de Pater, I., Conrad, A., Le Mignant, D., Chaffee, F., Gavel, D., 2003a. Searching and studying asteroids with AO systems. *BAAS*, 35, 959.

Marchis, F., Descamps, P., Hestroffer, D., Berthier, J., Vachier, F., Boccaletti, A., de Pater, I., Gavel, D., 2003b, A three-dimensional solution for the orbit of the asteroidal satellite of 22 Kalliope. *Icarus*, 165, 112-120.

Marchis, F., Berthier, J., Descamps, P., Hestroffer, D., Vachier, F., Laver, C., de Pater, I., Gavel, D.T., 2004. Studying binary asteroids with NGS and LGS AO systems. *Advancements in Adaptive Optics*. Edt. By Domenico B. Calia, Brent L. Ellerbroek, and Roberto Ragazzoni. *Proceedings of the SPIE*, 5490, 338-350.

Marchis, F., Baek, M., Berthier, J., Descamps, P., Hestroffer, D., Kaasalainen, M., Vachier, F., 2006. Large adaptive optics of asteroids (LAOSA): Size, shape, and occasionally density via multiplicity. *Workshop on Spacecraft Reconnaissance of Asteroid and Comet Interiors (2006)*, Abstract #3042.

Marchis, F., Baek, M., Berthier, J., Descamps, P., Hestroffer, D., Vachier, F., Colas, F., Lecacheux, J., Reddy, V., Pino, F., 2007a. (617) Patroclus. *CBET* 836,1. Edt. By Green, D.W.E.

Marchis, F., Descamps, P., Berthier, J., Hestroffer, D., Vachier, F., and A.W., Harris, 2007b. Main belt binary asteroidal systems with circular orbits. Submitted to *Icarus*.

Minnaert, M, 1941. The reciprocity principle in lunar photometry. *Astrophys. J.*, 93, 403-410.

Mottola, S., and Lahulla, F., 2000. Mutual eclipse events in asteroidal binary system 1996 FG3. Observations and a numerical model. *Icarus*, 146, 556-567.

Noll, K., 2006. Solar System binaries. Asteroids, Comets, Meteors, Proceedings of the 229th Symposium of the International Astronomical Union held in Búzios, Rio de Janeiro, Brasil Brazil August 7-12, 2005, Edited by Daniela, L., Sylvio Ferraz, M., Angel, F. Julio Cambridge: Cambridge University Press, 301-318.

Pravec, P., and G. Hahn, 1997. Two-period lightcurve of 1994 AW1: Indication of a binary asteroid ? *Icarus*, 127, 431-440.

Pravec, P., Wolf, M., and L. Šarounová, 1998. Occultation/eclipse events in binary asteroid 1991 VH. *Icarus*, 133, 79-88.

Pravec, P., Scheirich, P., Kušnirák, P., Šarounová, L., Mottola, S., Hahn, G., Brown, P., Esquerdo, G., Kaiser, N., Krzeminski, Z., Pray, D. P., Warner, B. D., Harris, A. W., Nolan, M. C., Howell, E. S., Benner, L. A. M., Margot, J.-L., Galád, A., Holliday, W., Hicks, M. D., Krugly, Yu. N., Tholen, D., Whiteley, R., Marchis, F., Degraff, D. R., Grauer, A., Larson, S., Velichko, F. P., Cooney, W. R., Stephens, R., Zhu, J., Kirsch, K., Dyvig, R., Snyder, L., Reddy, V., Moore, S., Gajdoš, Š., Világi, J., Masi, G., Higgins, D., Funkhouser, G., Knight, B., Slivan, S., Behrend, R., Grenon, M., Burki, G., Roy, R., Demeautis, C., Matter, D., Waelchli, N., Revaz, Y., Klotz, A., Rieugné, M., Thierry, P., Cotrez, V., Brunetto, L., Kober, G., 2006. Photometric survey of binary near-Earth asteroids. *Icarus*, 181, 63-93.

Prinz, M., Nehru, C.E., and J.S., Delaney, 1982. Silicate Inclusions in Irons and Metal-Silicate Assemblages. *Lunar and Planetary Science*, 13, 632-633.

Prinz, M., Nehru, C.E., Weisberg, M.K., Delaney, J.S., Yanai, K., and H., Kojima, 1984. H Chondritic Clasts in a Yamato L6 Chondrite: Implications for Metamorphism. *Meteoritics*, 19, 292.

Rivkin, A.S., Howell, E.S., Britt, D.T., Lebofsky, L.A., Nolan, M.C., and D.D., Branston, 1995. 3- μ m spectrophotometric survey of M- and E-class asteroids. *Icarus*, 117, 90-100.

Rivkin, A.S., Lebofsky, L.A., Britt, D.T. and E.S., Howell, 1997. Three-Micron Survey of E- and M-class Asteroids: Final Results. *BAAS*, 29, 972.

Rivkin, A.S., Howell, E.S., Lebofsky, L.A., Clark, B.E., and D.T., Britt, 2000. The nature of M-class asteroids from 3 μ m observations. *Icarus*, 145, 351-368.

Ryan, W. H., Ryan, E. V. and C. T. Martinez, 2004. 3782 Celle: Discovery of a Binary System within the Vesta Family of Asteroids. *Planetary and Space Science*, 52, 1093-1101.

Soma, M., Hayamizu, T., Berthier, J., and J. Lecacheux, 2006. 22 Kalliope and 22 Kalliope I. CBET 732. Edt. By Green, D.W.E.

Tedesco, E.F., Noah, P.V., Noah, M., Price, S.D., 2002. The Supplemental IRAS Minor Planet

Survey. *Astron. J.* 123, 1056-1085.

Tsiganis, K., Gomes, R., Morbidelli, A., and H.F., Levison, 2005. Origin of the orbital architecture of the giant planets of the Solar System. *Nature*, 435, 4596461.

Weidenschilling, S.J., Paolicchi, P., Zappala, V. 1989. Do asteroids have satellites? In *Asteroids II*; Proceedings of the Conference, Tucson, AZ, Mar. 8-11, 1988 (A90-27001 10-91). Tucson, AZ, University of Arizona Press, 1989, p. 643-658.

Acknowledgements

This work was partially supported by the National Science Foundation Science and Technology Center for Adaptive Optics, and managed by the University of California at Santa Cruz under cooperative agreement No. AST-9876783. This material is partly based upon work supported by the national Aeronautics and Space Administration through the Science Mission Directorate Research and Analysis Programs number NNX07AP70G

Tables

Table 1:

List of the observers, their facilities as well as the observational conditions.

Observers	Observatory	Aperture (m)	Exposure Time and filter (s)	Average seeing (arcsec.)
Colliac, J.-F.	Farigourette Observatory 5°27'21"E 43°18'38"N	0.20	10 (Clear)	3
Descamps, P., Vachier, F.	Haute-Provence Observatory IAU code #911	1.20	30 (R)	3
Deviatkin, A., Verestchagina, I.A., Gorshanov, D.L.	Pulkovo Observatory IAU code #084 02:01:19E 59°46'15"N	0.32	120 (B) 60 (V) 30 (R) 60 (I)	5
Kryszczyńska, A., Polinska, M.	Borowiec IAU code #187 17°04'29"E 52°16'37"N	0.40	180 (Clear)	5
Marchis F., Wong, M.H.	Lick Observatory IAU code #662	1.00	10(R)	1.4
Pollock, J.	Appalachian State University, Rankin Science Observatory 81°40' 54"W 36°12' 50"N	0.40	30(R)	3
Romanishin, W.,	University of Oklahoma	0.40	60	3.5
Wiggins P.	IAU code #718 112°18'E 40°38'N	0.35	15 (Clear)	2 - 4

Table 2: Summary of the observations. The object 1 is referred to as Kalliope and the object 2 as Linus. The column “Event” describes whether an eclipse has been observed or not along with the type of the event. Each event is identified by a Id number.

Date	Id	UT Start	UT End	Duration	Event	Observer	Phase angle (°)
11/26/06	1	03:14:06	09:53:11	06:39:05	-	J. Pollock	10,6
11/27/06	2	23:58:50	06:08:20	06:09:30	-	J. Pollock	10,2
12/02/06	3	01:04:16	11:49:14	10:44:58	-	J. Pollock	8,2
12/13/06	4	23:45:05	11:23:18	11:38:13	-	J. Pollock	4,1
12/15/06	5	00:45:35	11:16:15	10:30:40	-	J. Pollock	3,5
12/19/06	6	00:40:36	07:59:13	07:18:37	-	J. Pollock	2,9
01/27/07	7	00:02:00	07:54:11	07:52:11	-	J. Pollock	15,6
02/22/07	8	02:08:32	05:31:55	03:23:23	-	W. Romanishin et al.	20,3
02/27/07	9	03:42:18	05:43:46	02:01:28	-	W. Romanishin et al.	21,1
02/28/07	10	02:31:55	07:17:57	04:46:02	-	P. Wiggins	21,1
03/03/07	11	02:32:37	06:46:43	04:14:06	-	P. Wiggins	21,3
03/04/07	12	03:16:28	07:36:09	04:19:41	-	P. Wiggins	21,3
03/05/07	13	02:53:46	07:39:00	04:45:14	-	P. Wiggins	21,4
03/06/07	14	00:09:23	05:08:12	04:58:49	-	J. Pollock	21,5
03/07/07	15	02:17:56	05:31:54	03:13:58	-	W. Romanishin et al.	21,5
03/07/07	16	23:58:50	06:08:20	06:09:30	1E2	J. Pollock	21,5
03/08/07	17	01:55:50	05:30:34	03:34:44	1E2	W. Romanishin et al.	21,5
03/07/07	18	02:56:17	08:39:04	05:42:47	-	P. Wiggins	21,5
03/09/07	19	02:23:30	08:28:05	06:04:35	-	P. Wiggins	21,6
03/10/07	20	00:00:20	04:00:04	03:59:44	-	J. Pollock	21,6
03/10/07	21	02:08:34	05:33:19	03:24:45	-	W. Romanishin et al.	21,6
03/11/07	22	03:14:22	08:00:27	04:46:05	-	P. Wiggins	21,7
03/12/07	23	06:05:33	07:35:49	01:30:16	-	P. Wiggins	21,7
03/16/07	24	18:34:31	00:58:15	06:23:44	2E1	P. Descamps et al.	21,7
03/17/07	25	01:35:36	05:14:20	03:38:44	2E1	W. Romanishin et al.	21,7
03/17/07	26	04:26:28	07:22:53	02:56:25	-	F. Marchis et al.	21,7
03/18/07	27	01:36:28	05:13:45	03:37:17	-	W. Romanishin et al.	21,7
03/18/07	28	03:03:07	06:03:56	03:00:49	-	F. Marchis et al.	21,7
03/18/07	29	02:32:43	07:11:53	04:39:10	-	P. Wiggins	21,7
03/19/07	30	02:51:20	07:27:04	04:35:44	-	P. Wiggins	21,7
03/23/07	31	02:34:44	07:40:41	05:05:57	-	P. Wiggins	21,6
03/25/07	32	00:25:40	05:01:01	04:35:21	-	J. Pollock	21,6
03/25/07	33	02:22:39	06:54:44	04:32:05	-	P. Wiggins	21,6
03/27/07	34	19:17:02	22:50:18	03:33:16	2E1	J.F. Colliac	21,5
03/27/07	35	20:43:36	22:58:09	02:14:33	-	A. Deviatkin et al.	21,5
03/27/07	36	20:46:01	23:00:00	02:13:59	-	A. Deviatkin et al.	21,5
03/27/07	37	20:47:34	23:01:09	02:13:35	-	A. Deviatkin et al.	21,5
03/27/07	38	20:48:49	23:02:45	02:13:56	-	A. Deviatkin et al.	21,5
03/27/07	39	19:08:35	23:56:14	04:47:39	2E1	A. Kryszczyńska et al.	21,5
04/03/07	40	03:03:20	06:47:46	03:44:26	-	P. Wiggins	21,2
04/04/07	41	02:40:22	04:52:29	02:12:07	-	P. Wiggins	21,2
04/06/07	41	02:40:06	06:37:52	03:57:46	-	P. Wiggins	21,0
04/07/07	42	02:44:48	06:29:21	03:44:33	-	P. Wiggins	21,0
04/09/07	43	02:56:46	06:54:17	03:57:31	-	P. Wiggins	20,8
04/09/07	44	00:32:55	05:14:13	04:41:18	-	J. Pollock	20,8

Table 3:

Observed magnitudes drops and times of eclipse ingress and egress for each event. They are inferred from the fit of the global model. Predicted times are also given. The subscripts 1 and 2 respectively stand for Kalliope and Linus. Corresponding astrometric positions of Linus with respect to the center of Kalliope are given as well.

Date	Type of event	Observed time of ingress (UTC)	Predicted time of ingress (UTC)	Observed time of egress (UTC)	Predicted time of egress (UTC)	Magnitude drop	Astrometric positions at ingress and egress	
							X (mas)	Y(mas)
03/08/07	1E2	1: 24±5'	1:14	4: 7±5'	3:49	0.054	245 ± 4 253 ± 4	71 ± 4 -52 ± 4
03/17/07	2E1	0: 46±5'	0:50	3: 8±5'	3:15	0.081	-196 ± 4 -199 ± 4	-56 ± 4 47 ± 4
03/27/07	2E1	23: 24±5'	22:23	-	0:38	0.055	-197 ± 4	-57 ± 4

Table 4:

Refined orbital elements of Linus after accounting for the derived astrometric positions at the eclipse ingresses and egresses (cf. Table 3). The initial solution is that published in Marchis et al. (2007). The updated solution however does not succeed in accurately retrieving the observed times of eclipses. Nodal and apsidal rates as well as the Keplerian mean motion were derived from the J_2 theoretical value inferred from the 3D shape model of this paper together with the new determination of the equivalent radius of Kalliope. No significant eccentricity was detected.

Orbital parameters	Linus
Period (days)	3.5954±0.0011
Observed mean motion (°/day)	100.128
Keplerian mean motion (°/day)	100.287
Nodal rate (°/day)	-0.15
Apsidal rate (°/day)	0.3
Semi-major axis (km)	1099±11
Pole solution in ECJ2000 (degrees) λ (longitude), β (latitude)	$\lambda = 197\pm 2^\circ$, $\beta = -3\pm 2^\circ$
Inclination (degrees)	99.4±0.5°
Periapsis Argument (degrees)	54.7±30°
Ascending node (degrees)	284.5± 2.0°
Time of pericenter (JD)	2452185.489±0.006
Mass (kg)	8.18±0.26x10 ¹⁸

Table 5:

List of the observers of stellar occultation by Kalliope, and geographic coordinates of their places of observation.

#ID	Observer's name	East Longitude	North Latitude	Altitude
		° ' "	° ' "	m
1	H. Sato	140 29 25.3	37 44 35.9	90
2	M. Kashiwagura	140 08 40.2	38 22 47.5	182
3	H. Tomioka	140 41 09.0	36 38 33.0	33
4	A. Yaeza	140 36 11.0	36 31 28.0	230
5	H. Okita et al.	140 39 24.7	38 13 10.2	300
6	M. Koishikawa et al.	140 45 53.3	38 16 19.9	100
7	M. Satou	140 59 12.8	37 24 03.8	58
8	S. Uchiyama	140 32 11.5	36 20 36.3	6
9	S. Suzuki	139 32 04.6	35 22 44.2	30
10	M. Sato	139 28 33.7	35 40 54.5	60
11	R. Aikawa	139 26 50.4	35 56 56.5	21
12	M. Yanagisawa	139 32 37.0	35 39 27.7	80
13	T. Tanaka	139 34 50.0	35 17 53.0	9
14	K. Kitazaki	139 33 41.2	35 42 36.9	66
15	E. Katayama	139 33 22.2	35 41 52.9	62
16	T. Ohkawa	139 31 03.2	35 35 13.3	39
17	T. Hayamizu	130 18 00.7	31 50 19.2	20
18	H. Takashima	139 58 06.0	35 49 51.0	28
19	H. Fukui	138 15 14.0	34 51 05.0	25
20	H. Suzuki	137 42 48.4	34 45 53.8	50
21	K. Kenmotsu	133 44 52.6	34 41 40.3	53
22	A. Asai	136 31 24.3	35 10 14.2	187
23	A. Hashimoto	139 01 59.6	35 58 04.5	355
24	A. Matsui	138 15 31.4	36 18 31.9	557
25	S. Uehara	140 07 04.2	36 05 11.2	30

Table 6:

Times of the disappearance (D) and reappearance (R) of the star as measured by the observers

#ID	Disappearing time	Reappearing time	Duration	Accuracy D	Accuracy R	Observer's comments
	h m s	h m s	s	s	s	
1	19 49 18.38	19 49 44.43	26.05	0.15	0.07	gradual: 0 ^s .30D, 0 ^s .13R
2	19 49 37.30	19 49 54.47	17.17	0.05	0.07	gradual: 0 ^s .10D, 0 ^s .13R
3	19 48 57.50	19 49 24.37	26.87	0.06	0.07	gradual: 0 ^s .07D, 0 ^s .10R
4	19 48 57.70	19 49 22.10	22.40	0.20	0.30	
5	19 49 27.80	19 49 53.60	25.80	0.20	0.20	
6	-	19 49 53.78	0.00	0.01	0.50	D cloudy
7	19 49 08.50	19 49 36.98	28.48	1.50	0.50	
8	19 48 57.64	19 49 18.02	20.38	0.04	0.04	
9	19 47 56.10	19 47 59.91	3.81	0.04	0.04	
10	19 48 02.50	19 48 05.70	3.20	0.30	0.20	
11	19 48 06.80	19 48 10.60	3.80	0.30	0.30	D gradual
12	19 48 00.46	19 48 05.37	4.91	0.10	0.10	gradual: 0 ^s .1D, 0 ^s .1R
13	19 47 54.90	19 47 59.00	4.10	0.500	0.50	
14	19 48 01.31	19 48 06.34	5.03	0.04	0.04	gradual: 0 ^s .06D, 0 ^s .06R
15	19 48 01.00	19 48 06.00	5.00	0.30	0.30	
16	19 48 01.40	19 48 04.50	3.10	0.50	0.50	

Table 7:

Analysis of the radiometric measurements of IRAS using the NEATM (Harris, 1998). Given our knowledge of the shape of Kalliope we can calculate the effective diameter at the time of the IRAS sightings (Fig. 14 and text). Using the 3-D model average diameter of 156 km, we obtain an effective diameter at the time of the IRAS sightings in agreement with the NEATM model, validating our analysis.

Observations	Pv, η	D_{NEATM} km	Pole-on effective diameter ² if $D_{\text{mean}}=156$ km km
IRAS1 1983 06 15	0.15, 0.74	175.	171
IRAS2 1983/06/15	0.20, 0.43	152 ¹	172
IRAS3 1983/6/19	0.15, 0.72	174	172
IRAS4 1983/6/19	0.14, 0.80	182	170

1. η unrealistic. Probably erroneous
2. Calculated on the basis of the 3D-shape model; the contribution of the Kalliope I Linus satellite has been removed.

Figures

Figure 1 :

Collected photometric lightcurves between November 2006 and April 2007. They were used to derive a new shape model from a powerful inversion method (Kaasalainen et al.,2001). Synthetic lightcurves reckoned from such a model have been overlapped. The ability of the model to globally mimic the observations with a deviation less than 0.02mag endorses its reliability.

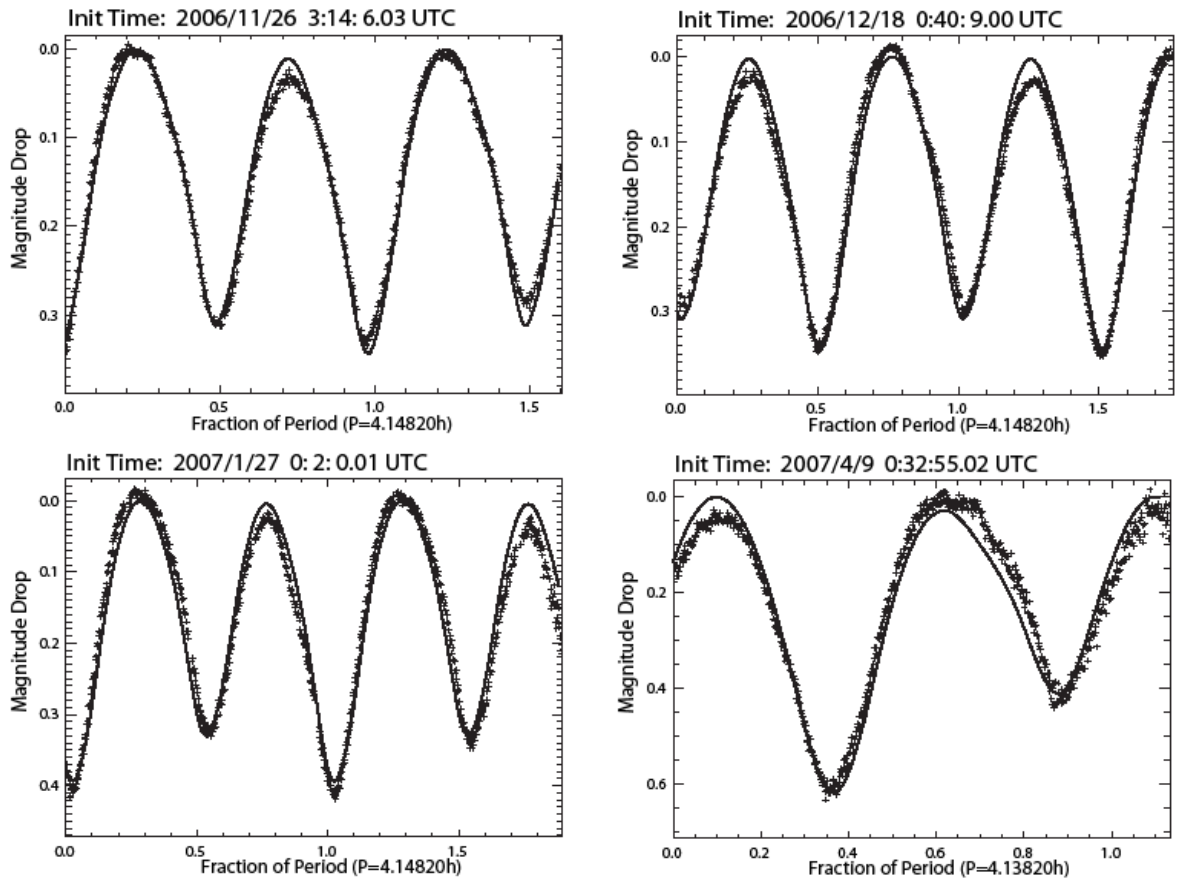


Figure 2 :

Side (*top*) and tip (*bottom*) views of the three-dimensional shape model of 22 Kalliope. As Kalliope was seen in a nearly edge-on aspect, hitherto never observed in such manner, the new model is consequently improved over the preceding one (Kaasalainen et al., 2002) with a slightly more elongated shape accounting for a peak-to-peak amplitude ranging from 0.35 to 0.55mag during this run. The J_2 term of the corresponding gravitational potential is of 0.19 assuming a uniform mass distribution.

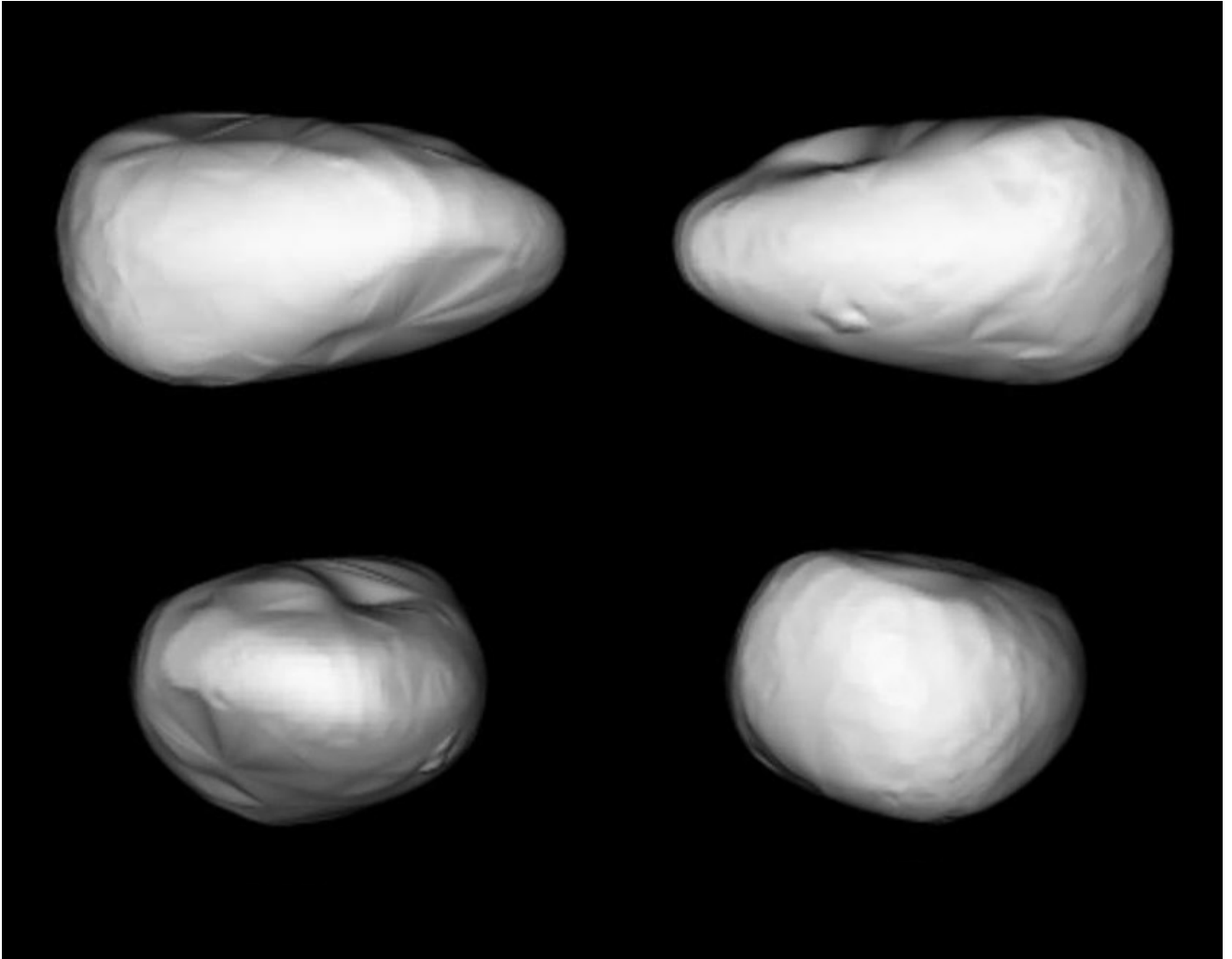


Figure 3:

Negative search for events. In order to detect an event, lightcurves taken during closer sessions are overlapped (left side). Their difference is plotted on the right side (see text for details). The reference run is plotted in plain line. The identification number of the involved runs refers to the ones given in table 2.

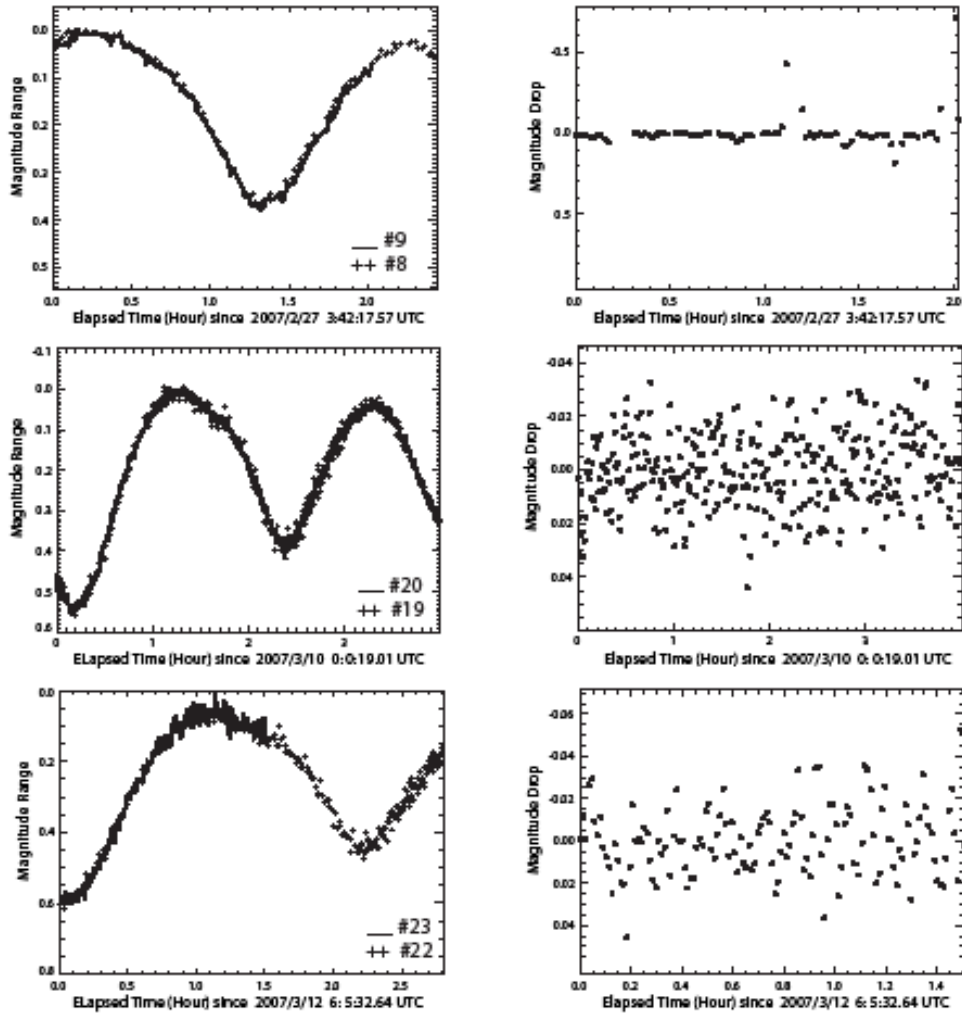


Figure 4

Negative search for events. In order to detect an event, lightcurves taken during closer sessions are overlapped (left side). Their difference is plotted on the right side (see text for details). The reference run is plotted in plain line. The identification number of the involved runs refers to the ones given in table 2.

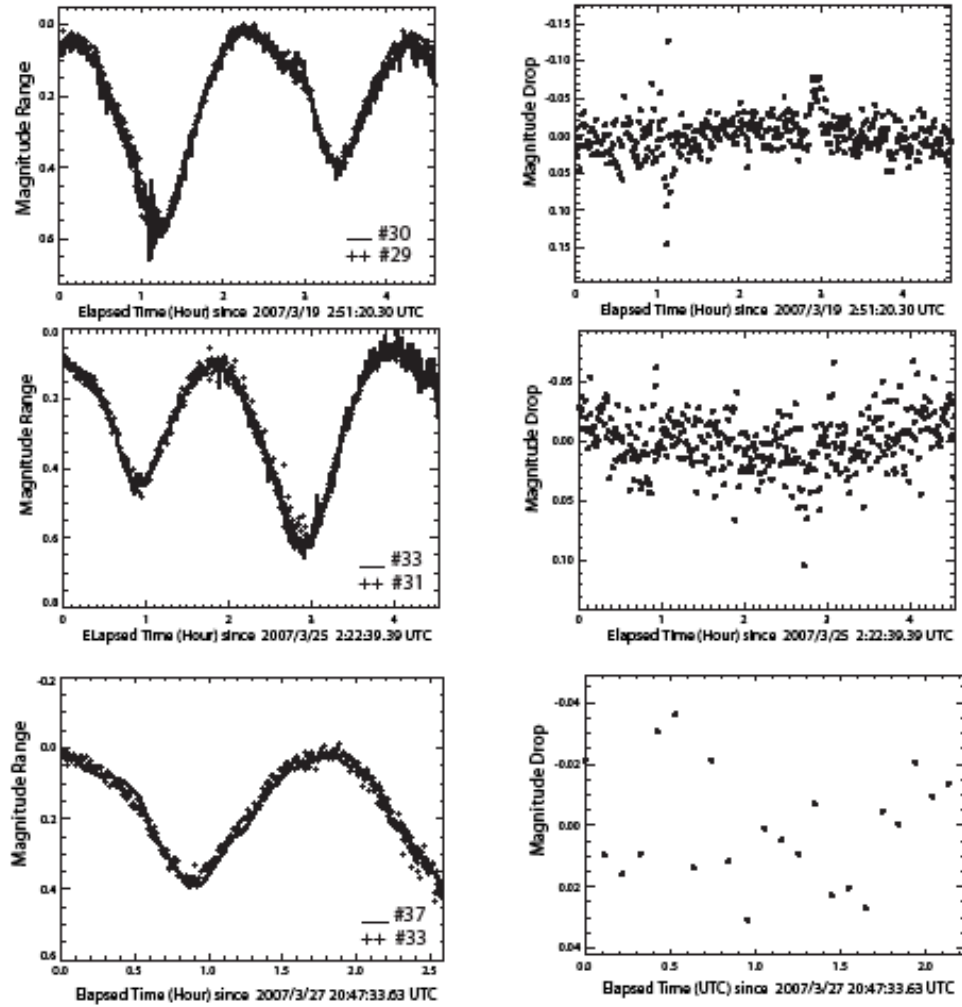


Figure 5

Positive detections of a total eclipse of Linus by Kalliope on 2007 March, 8. In order to detect an event, lightcurves taken during closer sessions are overlapped (left side). Their difference is plotted on the right side (see text for details). The reference run is plotted in plain line. The identification number of the involved runs refers to the ones given in table 2. The in-eclipse period of time is highlighted . The detection is performed from two different sites (#16 and #17) which confirms its reliability.

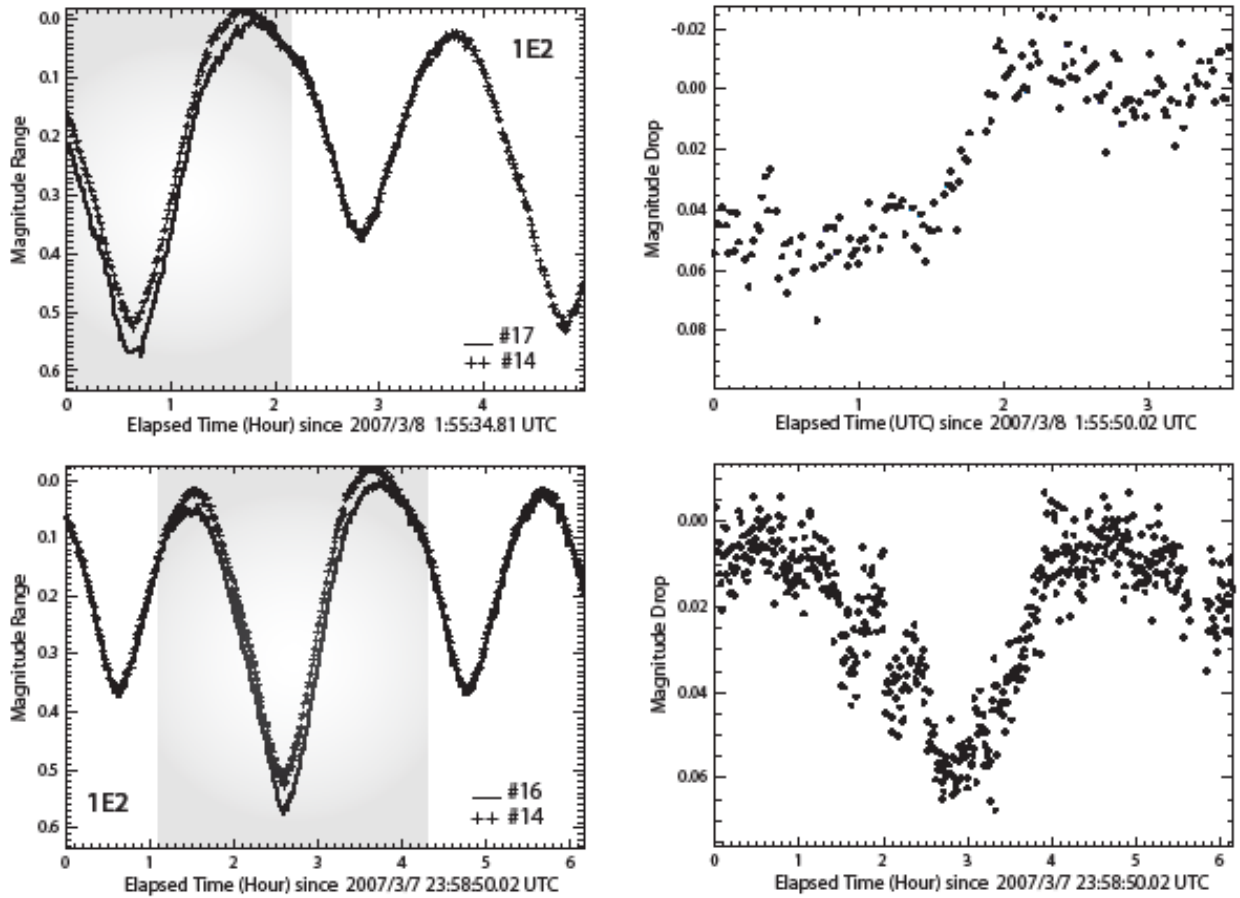


Figure 6

Positive detections of a total eclipse of Kalliope by Linus on 2007 March, 17. In order to detect an event, lightcurves taken during closer sessions are overlapped (left side). Their difference is plotted on the right side (see text for details). The reference run is plotted in plain line. The identification number of the involved runs refers to the ones given in table 2. The in-eclipse period of time is highlighted. The eclipse ingress is detected on the run #24 while the run #25 caught the end of the event.

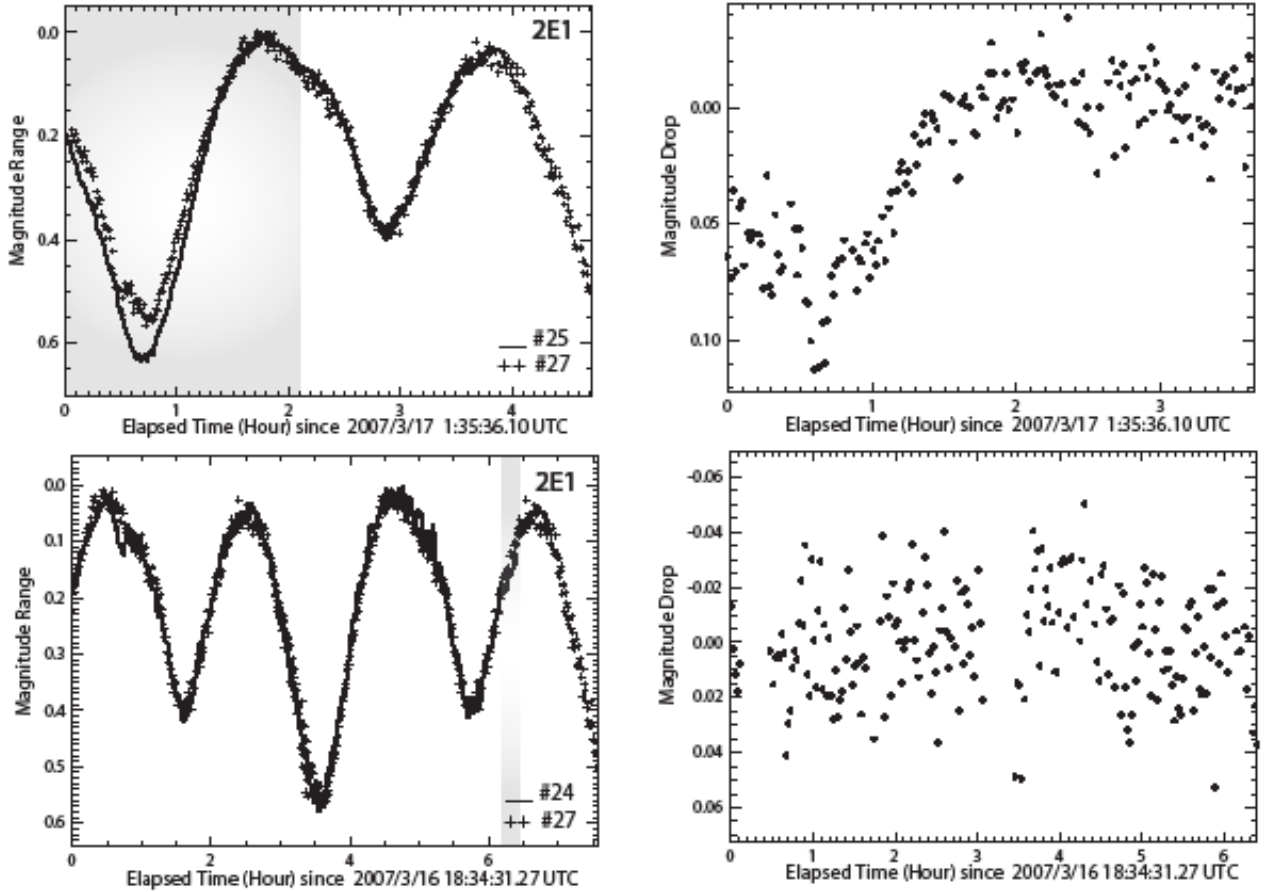


Figure 7

Positive detections of a total eclipse of Kalliope by Linus on 2007 March, 27. In order to detect an event, lightcurves taken during closer sessions are overlapped (left side). Their difference is plotted on the right side (see text for details). The reference run is plotted in plain line. The identification number of the involved runs refers to the ones given in table 2. The in-eclipse period of time is highlighted . The eclipse ingress is observed at the end of each positive runs (#34 and #39).

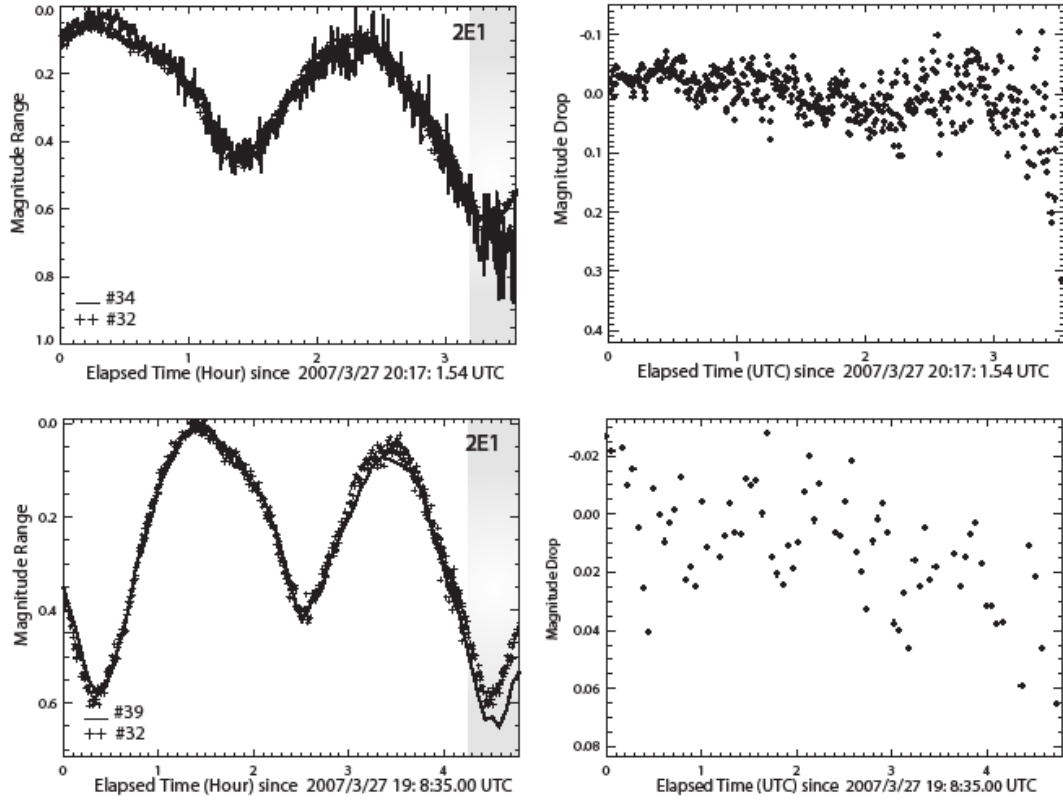


Figure 8:

Model of the eclipse of Kalliope by Linus of March, 17. The cylindrical umbra of Linus covers a substantial part of Kalliope owing to a significant macroscopic relief stretching of the shadow on the surface. This view may help to understand how different may be the level of light attenuation during an eclipse by Linus according to the topography of the surface of Kalliope facing Linus.

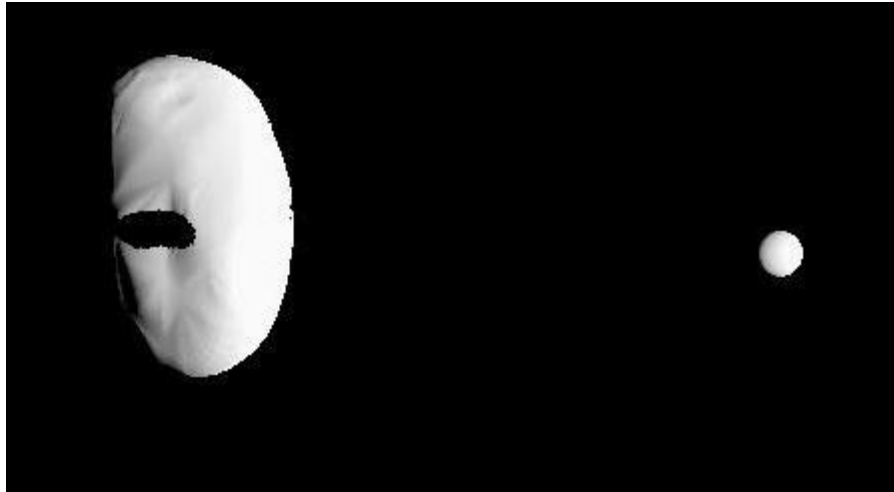


Figure 9

Study of the effects of the size parameters and the position of the orbit pole of Linus on the magnitude drop. These simulations are carried out for the two main detections of an eclipse event. See text for a discussion of these curves.

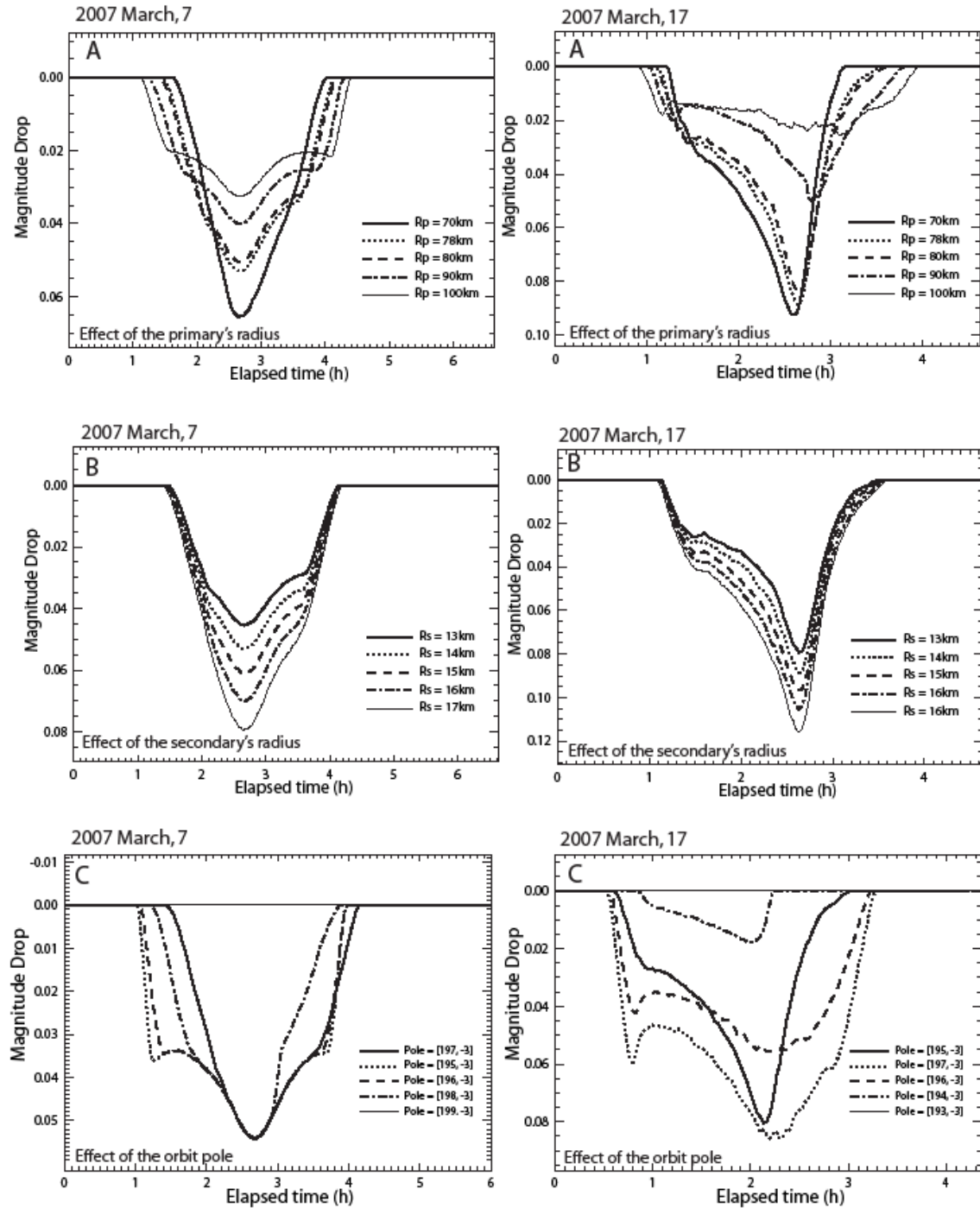


Figure 10

Synthetic curves of magnitude drop corresponding to the best-fit solution are superimposed to the positive detections shown on the figures 5, 6 and 7.

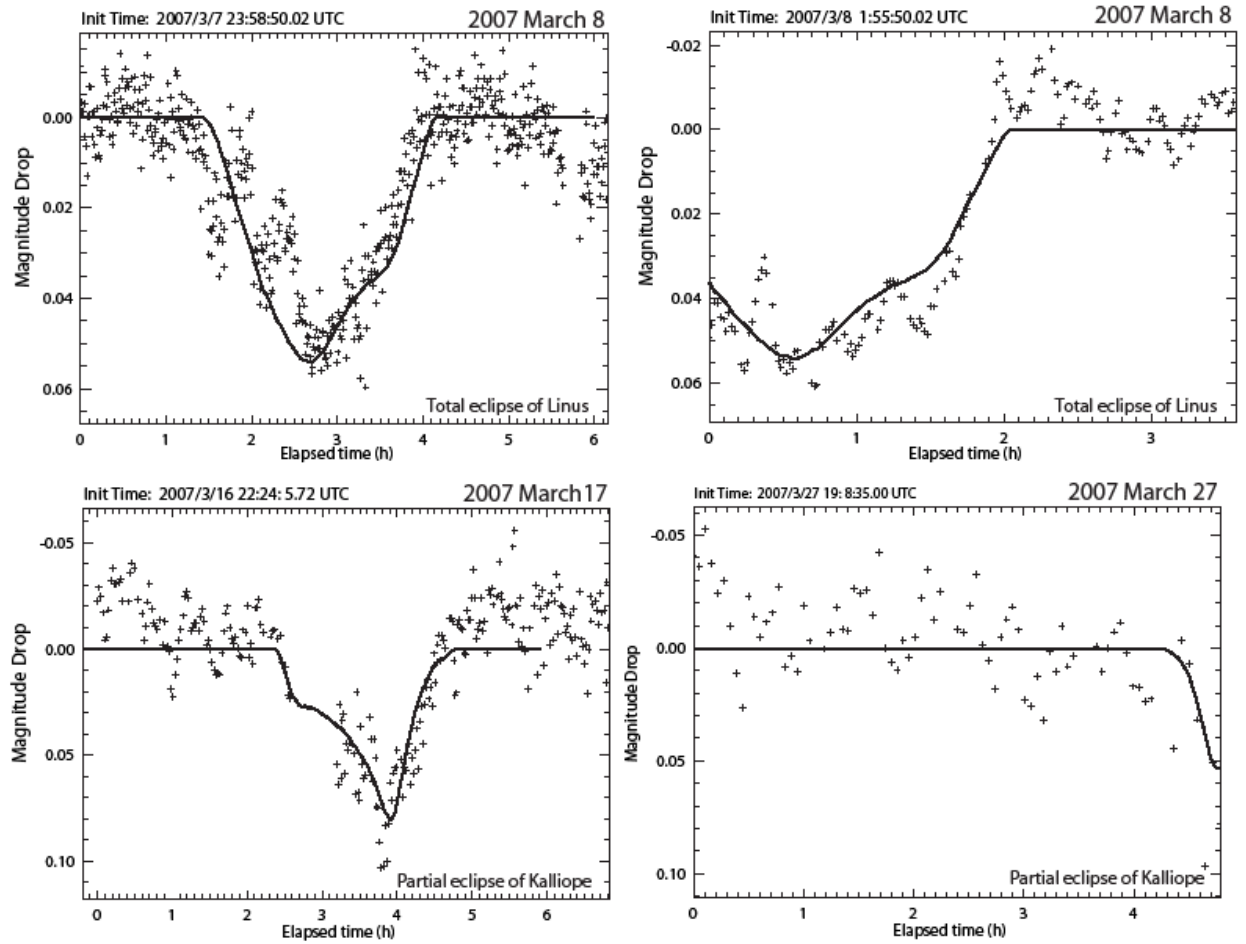


Figure 11

The left image displays an Adaptive Optics observation of Kalliope's primary recorded with the VLT-UT4 in June 2004 at $2.2\ \mu\text{m}$. The pixel scale is 13.25 milli-arcsec (mas), North is up and east is left. The right image corresponds to the projected shape of Kalliope's primary calculated using the shape model of this work and the pole solution ($\lambda = 197^\circ$ and $\beta = -3^\circ$ in ECJ2000). Despite the limited angular resolution with the AO observations ($\sim 65\ \text{mas}$), the appearance of Kalliope and the model are in excellent agreement.

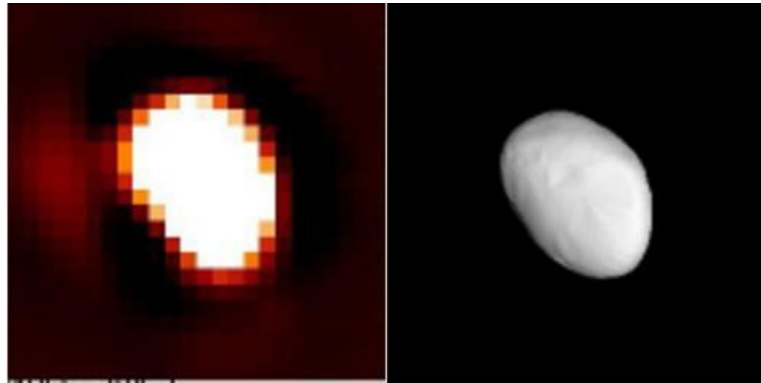


Figure 12 :

In the uppermost figure are plotted the equivalent chords of Kalliope and Linus as observed by the Japanese observers network (Soma et al., 2006) together with the expected position of Linus. Dashed straight lines refers to negative reports. In the close-up view of Kalliope (left bottom), IRAS size based (dashed line) and 78km-based (plain line) cross sections of Kalliope, deriving from our shape model (see Fig.2), are superimposed to the observed chords. It gives evidence that IRAS size significantly overestimates the real size of Kalliope. The close-up view of Linus (right bottom) shows elliptical profile of Linus (plain line) fitted to the chords. The dashed curves shows the uncertainty on the fitted profile of Linus.

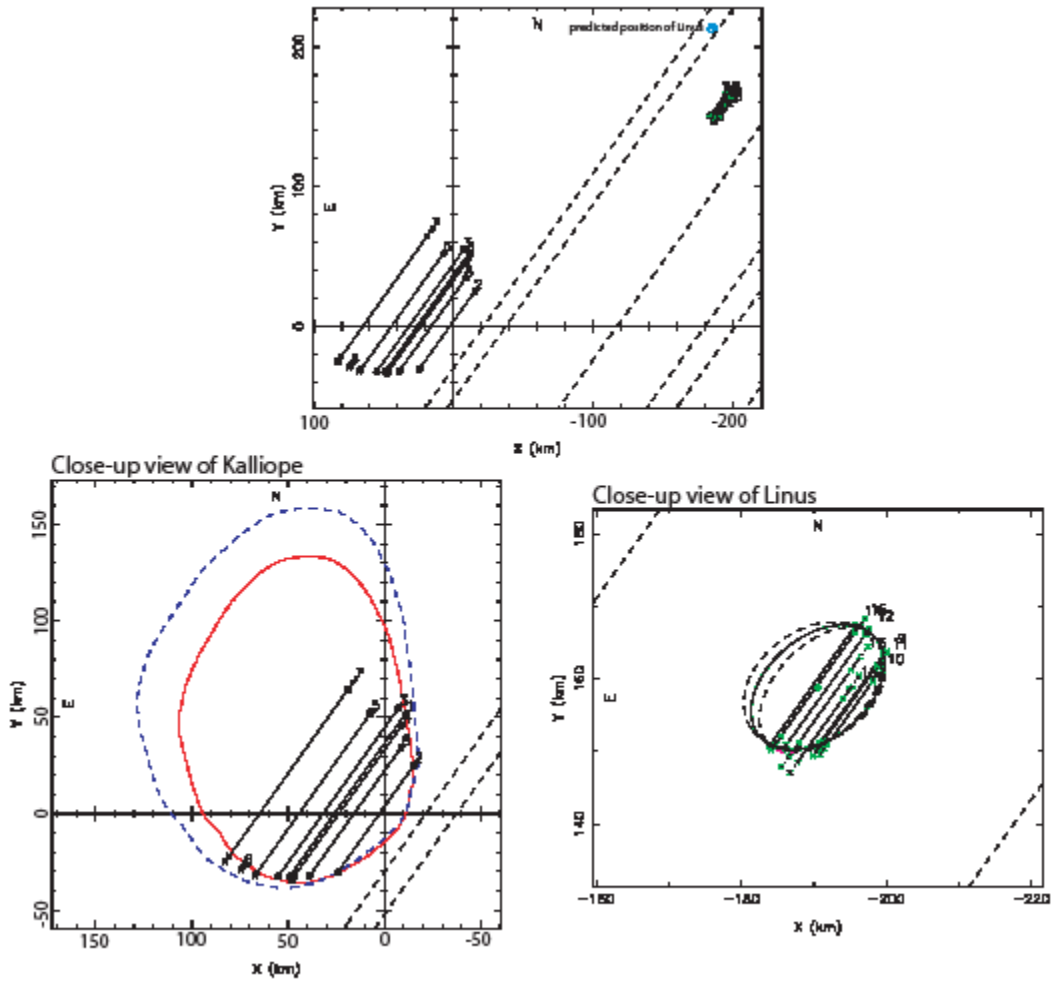


Figure 13

Apparent projected shape of Kalliope's primary during the IRAS sightings (June 15,19 1983) obtained using our pole solution and 3D-shape model. The asteroid was observed pole-on and exhibited its maximum apparent shape. The diameter (177 km see Table 7) derived from the IRAS sightings is therefore significantly larger than the true mean diameter.

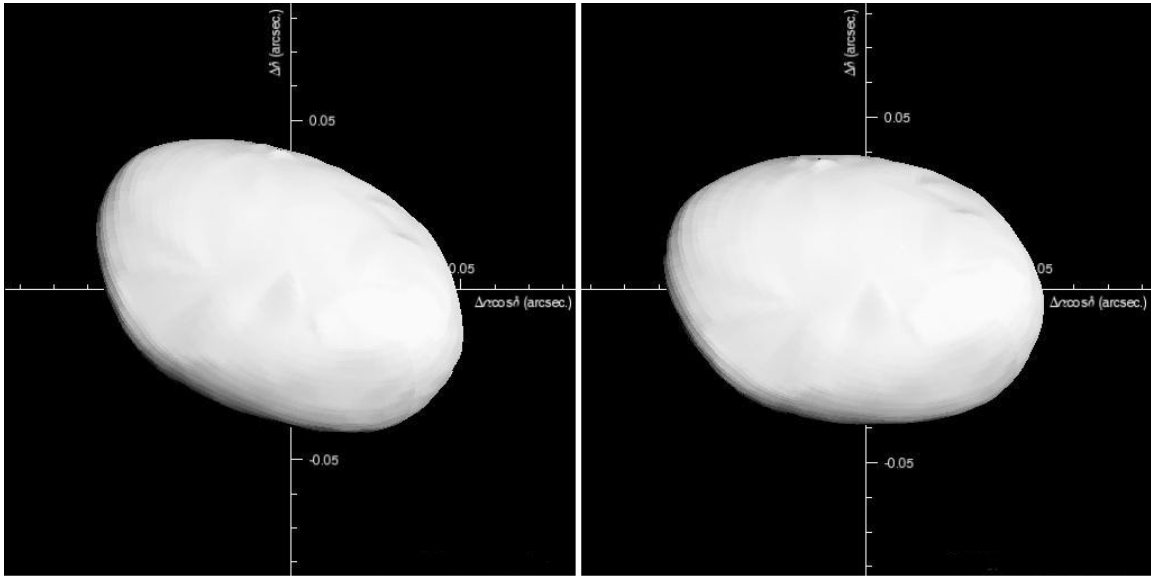


Figure 14

Diagram of the relative separation a/R_p against the mass ratio q after Weidenschilling et al. (1989). Curves of a same evolution time are plotted. They assume initial $a/R=1$, $\mu Q \approx 3 \times 10^{13} \text{ dynes/cm}^2$, $\rho = 4.09 \text{ g/cm}^3$, $R_p = 156 \text{ km}$ which are the physical characteristics of Kalliope derived in the present work. Binaries to the left of the curve labelled synchronous stability cannot maintain spin-orbit synchronism. The locus of Kalliope in this diagram is indicative of a very primitive body with a probable origin in the early Solar System.

